Analysis and Mitigation of Biases in Greenland Ice Sheet Mass Balance Trend Estimates From GRACE Mascon Products

Ran, Jiangjun; Ditmar, Pavel; Liu, Lin; Xiao, Yun; Klees, Roland; Tang, Xueyuan

DOI
10.1029/2020JB020880

Publication date
2021

Document Version
Final published version

Published in
Journal of Geophysical Research: Solid Earth

JGR Solid Earth

RESEARCH ARTICLE
10.1029/2020JB020880

Analysis and Mitigation of Biases in Greenland Ice Sheet Mass Balance Trend Estimates From GRACE Mascon Products

Jiangjun Ran[1,2], Pavel Ditmar[3], Lin Liu[4], Yun Xiao[5], Roland Klees[3], and Xueyuan Tang[6]

[1]Shenzhen Key Laboratory of Deep Offshore Oil and Gas Exploration Technology, Southern University of Science and Technology, Shenzhen, China, [2]Department of Earth and Space Sciences, Southern University of Science and Technology, Shenzhen, China, [3]Department of Geoscience and Remote Sensing, Delft University of Technology, Delft, The Netherlands, [4]Earth System Science Programme, Faculty of Science, The Chinese University of Hong Kong, Hong Kong, China, [5]Xi'an Research Institute of Surveying and Mapping, Xi'an, China, [6]Key Laboratory of Polar Science of Ministry of Natural Resources (MNR), Polar Research Institute of China, Shanghai, China

Key Points:

- State-of-the-art GRACE mascon solutions show obvious discrepancies in Greenland mass anomalies over the period 2003–2014 (e.g., reaching the level of 100–200 Gt)
- The major cause of the large discrepancies is likely caused by different spatial constraints
- We recommend that no smoothing constraints are applied to neighboring mascons across drainage system boundaries

Supporting Information:

Supporting Information may be found in the online version of this article.

Correspondence to:

J. Ran,
ranjj@sustech.edu.cn

Citation:

Ran, J., Ditmar, P., Liu, L., Xiao, Y., Klees, R., & Tang, X. (2021). Analysis and mitigation of biases in Greenland ice sheet mass balance trend estimates from GRACE mascon products. *Journal of Geophysical Research: Solid Earth*, *126*, e2020JB020880. https://doi.org/10.1029/2020JB020880

Received 30 AUG 2020
Accepted 26 JUN 2021

Abstract Mascon products derived from Gravity Recovery and Climate Experiment satellite gravimetry data are widely used to study the Greenland ice sheet mass balance. However, the products released by different research groups—JPL, CSR, and GSFC—show noticeable discrepancies. To understand them, we compare those mascon products with mascon solutions computed in-house using a varying regularization parameter. We show that the observed discrepancies are likely dominated by differences in the applied regularization. Furthermore, we present a numerical study aimed at an in-depth analysis of regularization-driven biases in the solutions. We demonstrate the ability of our simulations to reproduce 60%–80% of biases observed in real data, which proves that our simulations are sufficiently realistic. After that, we demonstrate that the quality of mascon-based estimates can be increased by a proper modification of the applied regularization: no correlation between mascons is assumed when they belong to different drainage systems. Using both simulations and real data analysis, we show that the improved regularization mitigates signal leakage between drainage systems by 11%–56%. Finally, we validate various mascon solutions over the SW drainage system, using trends from (i) the GOCO-06S model and (ii) the Input-Output Method as control data. In general, the in-house computed trend estimates are consistent with the trends from CSR and JPL solutions and the trends from the control data.

Plain Language Summary The mass variations of Greenland ice sheet (GrIS) have been widely monitored by the satellite mission named Gravity Recovery and Climate Experiment (GRACE). Currently, there are different research groups (i.e., JPL, CSR, and GSFC), which produce various mascon products from the GRACE data. Noticeable discrepancies, however, are shown in these mascon products. In this study, we try to analyze the reasons that cause the discrepancies, by varying with different strengths of regularization when estimating the mascon products using our variant of the mascon approach. Using both real data and simulation, we show that the observed discrepancies are likely dominated by differences in the applied regularization. Thereafter, we find that by utilizing a proper modification of the spatial constraint, the quality of the mascon estimates in GrIS can be obviously improved by 11%–56%. Finally, the trend estimates of the SW drainage systems from the GOCO-06S model and the Input-Output Method are utilized as independent data, to validate the mascon-based solutions. It is found that the trends from CSR, JPL, and the estimates by the modified spatial constraints are in good agreement with the independent data.

1. Introduction

The Gravity Recovery and Climate Experiment (GRACE) satellite mission, which was launched in 2002, allowed mass anomalies at the global and regional scale to be estimated until June 2017 (Tapley et al., 2004, 2019). Those estimates have become one of the most valuable data sources being used to understand mass transport in the Earth system. Several research areas benefit from this information, including hydrology (e.g., Landerer & Swenson, 2012; Ramillien et al., 2008; Rodell et al., 2004; Scanlon et al., 2016;

Schmidt et al., 2006; Syed et al., 2008; Wahr et al., 1998), cryosphere studies (e.g., Chen et al., 2006; Luthcke et al., 2013; Ran, Ditmar, Klees, et al., 2018; Schrama et al., 2014; Shepherd et al., 2012; Siemes et al., 2013; van den Broeke et al., 2009; Velicogna & Wahr, 2006; Velicogna et al., 2014, 2020; Wouters et al., 2008), and physics of the solid Earth (e.g., Chen et al., 2007; Han et al., 2006; Heki and Matsuo, 2010; Panet et al., 2007; W. Sun et al., 2009; Wang et al., 2012; etc.).

The GRACE-based mascon solutions offered by the Jet Propulsion Laboratory (JPL RL06 v01) (Watkins et al., 2015), the Goddard Space Flight Center (GSFC v2.4) (Luthcke et al., 2013; Rowlands et al., 2005), and the Center for Space Research (CSR RL06 v01) of The University of Texas at Austin (Save et al., 2016) are widely used. Compared to spherical harmonic solutions, they offer less signal leakage and a higher spatial resolution (Scanlon et al., 2016). The JPL mascon solutions used $3° \times 3°$ mascons, whereas the CSR and GSFC mascon solutions used equal-area mascons with a size of $1° \times 1°$ at the equator. Spatial and temporal constraints were used when computing the mascon solutions. For instance, GSFC used an exponential function describing correlations in time and space between mascon pairs (Luthcke et al., 2013), JPL used temporal and spatial constraints, which were extracted from geophysical and hydrological models (Watkins et al., 2015), and CSR used a temporally and spatially variable zero-order Tikhonov regularization, which implies no correlations in the spatial and time-domain (Save et al., 2016). From a mathematical point of view, all constraints can be considered as special variants of Tikhonov regularization (Tikhonov, 1963a, 1963b).

Overall, the mascon products from CSR, GSFC, and JPL show a good performance in observing the mass balance rate over the entire Greenland ice sheet(GrIS) (Ran, Ditmar, Klees, et al., 2018). However, there are significant differences at a drainage system scale. For instance, Figure 1 shows the mass anomaly time series for five different drainage systems of the GrIS. To avoid splitting individual mascons, each drainage system comprises an integer number of JPL mascons, because they have the largest size (i.e., $3° \times 3°$), as compared with other mascon products ($\sim 1° \times 1°$ for CSR and GSFC). Figure 1 reveals large temporal and spatial discrepancies between the mascon solutions of the three analysis centers. For instance, discrepancies between mass anomalies accumulated from 2003 to 2014 range from 100 to 200 Gt depending on the drainage system. In the southwest drainage system, the estimated mass balance rate over the years 2003–2006 is 7, 9, and −28 Gt/yr for CSR, JPL, and GSFC products, respectively.

In this study, we systematically investigate the discrepancies between different mascon products over the GrIS. We analyze the causes of those discrepancies by reproducing different behavior of mass anomaly time series using the variant of the mascon approach by Ran, Ditmar, Klees, et al. (2018) and Ran, Ditmar, and Klees (2018). Furthermore, we demonstrate that the quality of mascon-based estimates can be increased by a proper modification of the applied spatial constraints. The major assumption behind the improved spatial constraints exploited in this study is that there are no correlations between mascons belonging to different drainage systems. This assumption is driven by the fact that there is a negligible mass exchange between neighboring drainage systems, which implies that the behavior of mass anomalies in neighboring drainage systems may be very different. The assumption of no correlations between mascons belonging to different drainage systems may reduce signal leakage. A similar idea was already considered in Sabaka et al. (2010) and Luthcke et al. (2013), where Greenland was divided into two regions separated by the 2,000 m elevation line. They assumed the absence of correlations between mass variations in the two regions. However, those constraints did not facilitate a reduction of signal leakage between neighboring drainage systems.

The study is organized as follows. In Section 2, we present the methodology, including the adopted mascon approach and the improved spatial constraints. The data utilized in this study are introduced in Section 3. In Section 4, the discrepancies between the CSR, JPL, and GSFC mascon products and the results obtained with the improved spatial constraints are quantified and analyzed. The discussion and conclusions are left for Sections 5 and 6, respectively.

2. Methods

To analyze the mass anomaly time series from the CSR, GSFC, and JPL mascon products, we compare them with the mass anomalies based on the variant of the mascon approach suggested in Ran, Ditmar, Klees, et al. (2018), Ran, Ditmar, and Klees (2018), and Ran, Vizcaino, et al. (2018). This approach is summarized

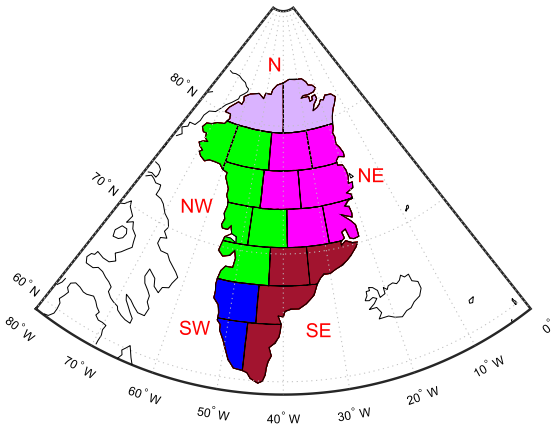

(a) Parameterization

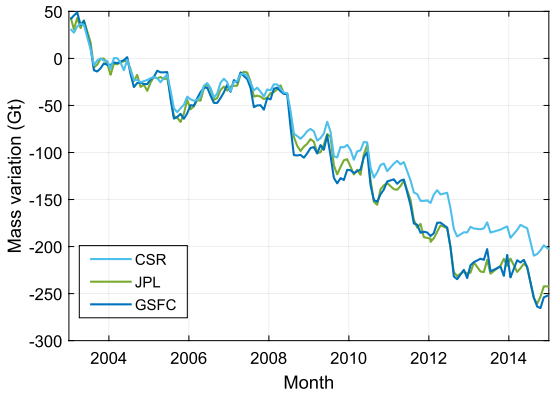

(b) N

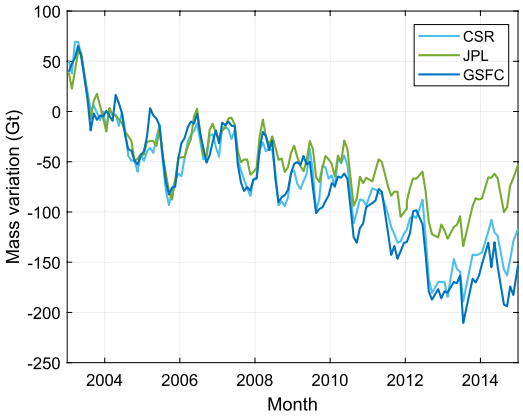

(c) NE

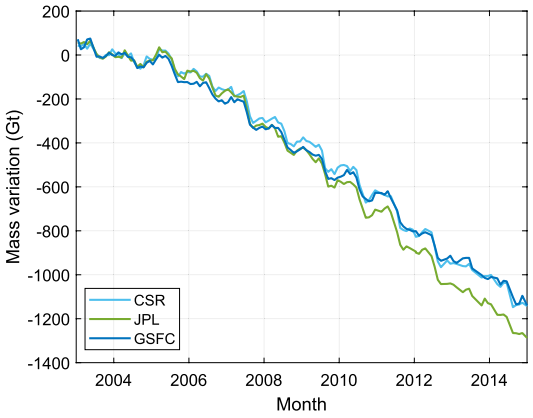

(d) NW

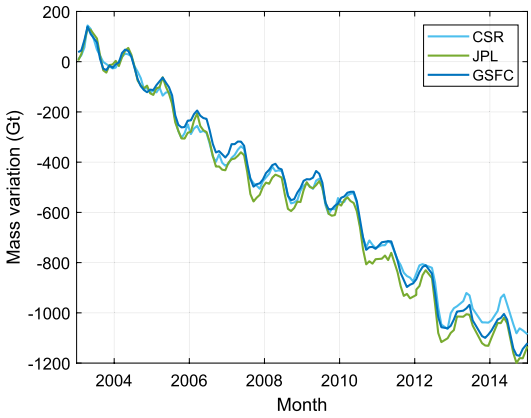

(e) SE

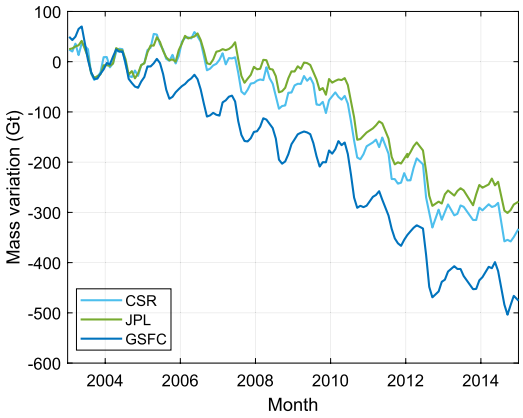

(f) SW

Figure 1. (a) The geometry of the drainage systems, aggregated from the JPL mascons. (b–f): Mass anomaly time series for five Greenland ice sheet drainage systems from CSR, JPL, and GSFC mascon solutions.

in Section 2.1. Furthermore, we consider the mass anomaly estimates obtained with improved spatial constraints in Section 2.2.

2.1. Variant of the Mascon Approach Adopted to Estimate Mass Anomalies

The mascon approach of Ran, Ditmar, Klees, et al. (2018) is an extension of the techniques proposed by Forsberg and Reeh (2007) and Baur and Sneeuw (2011). Like many other post-processing schemes developed so far (e.g., Bonin & Chambers, 2013; Jacob et al., 2012; Sasgen et al., 2010; Schrama & Wouters, 2011; Wouters et al., 2008), it uses GRACE Level-2 spherical harmonic solutions as starting point instead of GRACE Level-1B data, as used in the mascon solutions of GSFC (Luthcke et al., 2013), CSR (Save et al., 2016), and JPL (Watkins et al., 2015). The computations start from synthesizing "pseudo-observations"—gravity disturbances at a mean satellite altitude—from the monthly set of spherical harmonic coefficients (SHCs). The unknown parameters (surface density variations in kg/m^2 per mascon) are then estimated using weighted least square techniques. The solution is stabilized using first-order Tikhonov regularization. Finally, the estimated surface densities are converted into mass anomalies in units of Gt for visualization purposes (e.g., Figure 1). Note that opposite to Forsberg and Reeh (2007) and Baur and Sneeuw (2011), the full noise covariance matrices of monthly SHCs are propagated into the pseudo-observations using the law of covariance propagation, and used as inverse weight matrix in the weighted least square approach. Moreover, the columns of the design matrix are low-pass filtered to make them spectrally consistent with the spatial resolution of the monthly spherical harmonic models.

2.2. Adopted Spatial Constraints

To suppress the amplification of data noise when computing the mascon surface densities, Tikhonov regularization (Tikhonov, 1963a, 1963b) is used. The regularized least square solution is then given as

$$\hat{\boldsymbol{x}} = \arg\min_{\boldsymbol{x}}\left[\left(\boldsymbol{d}-\boldsymbol{A}\boldsymbol{x}\right)^{T}\boldsymbol{C}_{\boldsymbol{d}}{}^{-1}\left(\boldsymbol{d}-\boldsymbol{A}\boldsymbol{x}\right)+\alpha\Phi\left(\boldsymbol{x}\right)\right], \tag{1}$$

where $\Phi\left(x\right)$ is the Tikhonov regularization functional and α is the regularization parameter. The solution of Equation 1 can be written as

$$\hat{\boldsymbol{x}} = \left(\mathbf{A}^{\boldsymbol{T}}\mathbf{C}_{\boldsymbol{d}}{}^{-1}\mathbf{A}+\alpha\mathbf{R}'\right)^{-1}\mathbf{A}^{\boldsymbol{T}}\mathbf{C}_{\boldsymbol{d}}{}^{-1}\boldsymbol{d}, \tag{2}$$

where $\mathbf{A}$ is the design matrix, $\boldsymbol{d}$ is the vector of pseudo observations, $\boldsymbol{C_d}$ is the noise covariance matrix of $\boldsymbol{d}$, and $\mathbf{R}'$ is the regularization matrix associated with the minimization functional $\Phi\left(x\right)$. There are different choices of $\Phi\left(x\right)$ (see Text S1). For instance, zero-order Tikhonov regularization minimizes the L2-norm of the surface density function, whereas first-order Tikhonov regularization minimizes the L2-norm of the gradient of that function. For the application at hand, we prefer to use first-order Tikhonov regularization as zero-order Tikhonov regularization may heavily damp long-term trends and other strong signals (Ran, 2017).

The implementation of the first-order Tikhonov spatial constraints depends on the panelization of the GrIS with mascons and is similar to the one by Ran, Ditmar, Klees, et al. (2018) and Watkins et al. (2015). The territory of GrIS is covered by non-overlapping mascons, which are defined in two steps. First, the GrIS is subdivided into latitudinal bands. Second, each latitudinal band is subdivided into mascons along meridians to obtain mascons of similar areas. As shown in Figure 1a, the mascons do not form an equal-angular grid. This makes the implementation of the ordinary first-order Tikhonov regularization more intricate. To explain the implementation, we consider seven mascons with labels h, i, j, k, l, m, and n (see Figure 2a) and denote the corresponding surface mass densities as $\boldsymbol{x}_h, x_i, x_j, x_k, x_l, x_m$, and x_n. To minimize the north-south component of the horizontal gradient, the mascons with indices h, i, k, m, and n, need to be formally divided into sub-mascons (cf., Figure 2b). The sub-mascons share the same surface density with the parent mascon, and only serve to implement the spatial constraint associated with the first-order Tikhonov regularization.

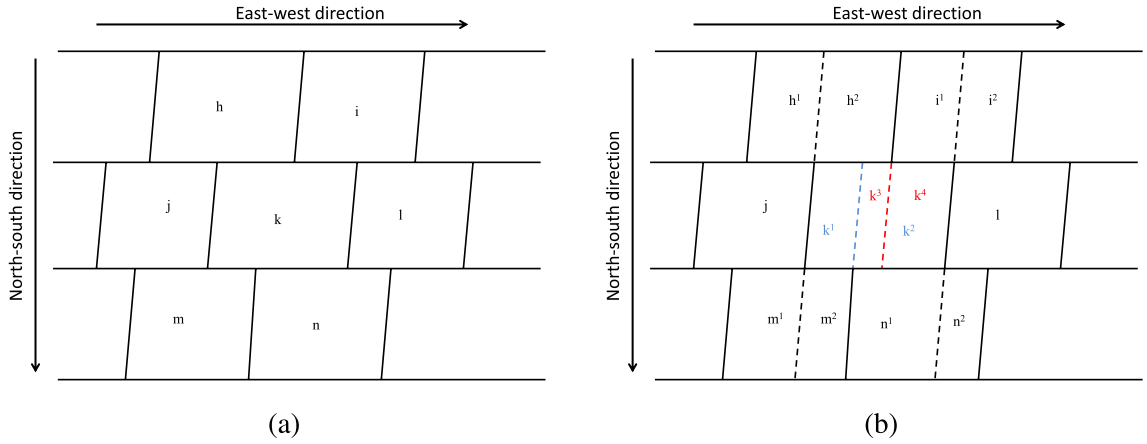

Figure 2. (a) Schematic mascon distribution in the inner part of Greenland, and (b) division of mascons into sub-mascons to compute the elements of the first-order Tikhonov regularization matrix. *h, i, j, l, m*, and *n* are the indexes of the mascons that are neighbors of mascon *k*. Based on the boundaries of neighboring mascons, mascon *k* is virtually divided into k^1, and k^2, or k^3 and k^4. Similar divisions are also applied to the neighboring mascons *h*, *i*, *m,* and *n*.

For instance, $\boldsymbol{x}_k = \boldsymbol{x}_{k^1} = x_{k^2} = x_{k^3} = x_{k^4}$. Therefore, the minimization condition that involves mascon *k* shown in Figure 2 can be written, in line with Equation S4, as:

$$\begin{aligned}\Phi_1(x) = \sum_k \Bigg[& \underbrace{f_{h^2k^3}\left(x_{h^2} - x_{k^3}\right)^2 + f_{i^1k^4}\left(x_{i^1} - x_{k^4}\right)^2 + f_{k^1m^2}\left(x_{k^1} - x_{m^2}\right)^2}_{\text{North-south direction}} \\ & + \underbrace{f_{k^2n^1}\left(x_{k^2} - \boldsymbol{x}_{n^1}\right)^2}_{\text{North-south direction}} + \underbrace{f_{jk}\left(x_j - x_k\right)^2 + f_{kl}\left(x_k - x_l\right)^2}_{\text{East-west direction}} \Bigg] \\ = & \sum_k \sum_{k'} R_{kk'} x_k x_{k'} = \boldsymbol{x}^T \boldsymbol{R} \boldsymbol{x},\end{aligned} \tag{3}$$

with $f_{jk} = \text{area}_j + \text{area}_k \,/\, 2 \,/\, d_{jk}^2$, where d_{jk} is the distance between the centers of mascons *j* and *k*; whereas $area_j$ and $area_k$ are the areas of mascon *j* and *k*, respectively. The non-zero elements of the first-order Tikhonov regularization matrix associated with the *k*th mascon are given in Table 1. Notice that all the

Table 1
First-Order Tikhonov Regularization Matrix Elements Associated With the k-th Mascon and Its Neighbors (cf., Figure 2)

patch ID		*h*	*i*	*j*	*k*	*l*	*m*	*n*	...
...	...	...	...	...	...	...	...	...	...
h	...				$-f_{h^2k^3}$				...
i	...				$-f_{i^1k^4}$				...
j	...				$-f_{jk}$				...
k	...	$-f_{h^2k^3}$	$-f_{i^1k^4}$	$-f_{jk}$	$f_{h^2k^3} + f_{i^1k^4} + f_{k^1m^2} + f_{k^2n^1} + f_{jk} + f_{kl}$	$-f_{kl}$	$-f_{k^1m^2}$	$-f_{k^2n^1}$	...
l	...				$-f_{kl}$				...
m	...				$-f_{k^1m^2}$				...
n	...				$-f_{k^2n^1}$				...
...	...	...	...	...	...	...	...	...	...

non-zero off-diagonal elements correspond to the neighbors of the kth mascons (i.e., the mascons that have a common side with the kth mascon).

The general expression for the elements R_{ki} can be written as follows:

$$R_{ki} = \begin{cases} -f_{k'i'} & \text{if } k \neq i, k \text{ has a common side with } i \\ \sum_j f_{j'k'} & \text{if } k = i \\ 0 & \text{otherwise} \end{cases} \quad (4)$$

where i' is the part of the ith mascon that shares the border with mascon k, whereas k' is the part of mascon k that shares the border with mascon i. Summation index j runs over the neighbors of the kth mascon (again, the "prime" symbol indicates the mascon parts in a given pair that have a common border). It is worth to stress that the sub-mascons are introduced only "virtually" (i.e., each mass anomaly is estimated as a single number for the entire mascon; mass anomalies in kg/m^2 for all the sub-mascons within a given mascon are the same).

By now, we considered the "ordinary" first-order Tikhonov regularization, which covers all pairs of neighboring masons. As far as the improved spatial constraint is concerned, the major assumption behind it is that there is no correlation between mascons that belong to different drainage systems. This is implemented as an update of the regularization matrix **R** of Equation 4. This update only considers pairs of mascons as neighbors if they belong to the same drainage system. Hence, correlations between pairs of mascons that belong to different drainage systems are set equal to zero, which reduces signal leakage between the corresponding mascons.

3. Data

3.1. GRACE

As input, we use the CSR Release 6 (RL06) GRACE SHC solutions which are complete to degree 96 and provided with full noise covariance matrices. The time interval considered in this study covers the years from 2003 to 2014. As no sets of SHCs are provided for 15 months, the data set comprises 141 monthly solutions. The monthly $C_{2,0}$ coefficients are replaced by SLR-based ones (Loomis et al., 2020). The missing degree-one coefficients are taken from Y. Sun et al. (2016). For that reason, noise correlations between the degree-1 coefficients and the $C_{2,0}$ coefficients on the one hand and all other coefficients on the other hand are assumed to be zero. The glacial isostatic adjustment is corrected for using the model from Peltier et al. (2015), which was also used when computing the mascon solutions of CSR RL06, JPL RL06, and GSFC v2.4.

3.2. RACMO2.3

To validate GRACE-based estimates of mass variations, we use RACMO2.3, a regional atmospheric climate model developed by the Royal Netherlands Meteorological Institute (KNMI) and the Institute for Marine and Atmospheric Research (IMAU) at Utrecht University (Noël et al., 2015). More specifically, we use Surface Mass Balance (SMB) estimates over 11-by-11 km blocks with daily temporal resolution. The daily SMB estimates are time-integrated to provide cumulative SMB mass anomalies; averaging provides mean monthly mass anomalies.

4. Results

4.1. Understanding the Discrepancies Between the CSR, JPL, and GSFC Mascon Products

Figures 3 and S2 show the GrIS mass variations per drainage system from CSR, JPL, and GSFC mascon solutions. Though differences are relatively small at the beginning of the period, they increase monotonically as function of time and attain several hundreds of Gts at the end of the period. To understand the cause of these discrepancies, we computed different sets of mascon-type estimates (referred as "TUD-SUSTech" in this study) using the mascon approach of Ran, Ditmar, Klees, et al. (2018) in combination with the

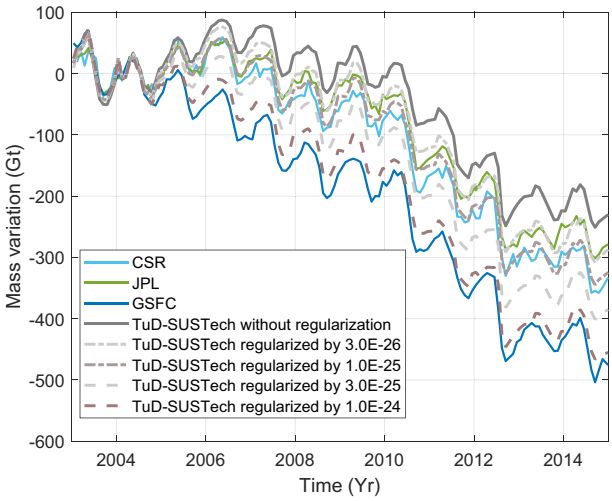

Figure 3. Mass anomaly time series for the SW drainage system based on the mascon products from CSR, JPL, and GSFC, as well on TUD-SUSTech mascon solutions produced with different regularization parameters (from 0 to 10^{-24}). For other drainage systems, please see Figure S2.

ordinary first-order Tikhonov regularization of Equation 4. On the one hand, the differences between the TUD-SUSTech solutions, and on the other hand, the CSR, JPL, and GSFC solutions depend on the choice of the regularization parameter of the TUD-SUSTech solution (cf., Figures 3 and S2). In general, we find that by changing the regularization parameter of the TuD-SUSTech mascon solutions, we can mimic the mascon solutions from CSR, JPL, and GSFC reasonably well. This is done per drainage system.

Figure 4 shows per drainage system the RMS difference between each of the JPL, CSR, and GSFC solutions and the TUD-SUSTech solutions as function of the regularization parameter for the latter solution. The smallest RMS difference is about 20 Gt. Depending on the solution and the drainage system, the minimum RMS difference is attained for different regularization parameters.

In the SW drainage system (see Figures 3 and 4), the regularization parameters which provide the closest fit to the solutions of the analysis centers are 3×10^{-26} (JPL), 1×10^{-25} (CSR), and 1×10^{-24} (GSFC). The TUD-SUSTech solution without regularization shows a clear mass gain signal over the period 2004–2006, and provides the smallest mass loss trend over the full period. The mass gain over the period 2004–2006 becomes smaller with increasing regularization parameter and turns into a mass loss signal when the regularization parameter is large enough. We explain this behavior by signal leakage from the neighboring NW and SE drainage systems, which show large mass losses.

For the NW drainage system (see Figures 4 and S2), a regularization parameter of 3×10^{-26} gives the smallest RMS difference to the JPL solutions: of about 20 Gt. A similar fit to the CSR solutions is obtained with a significantly larger regularization parameter of 3×10^{-25}. The latter value of the regularization parameter also provides the best fit to the GSFC solutions, though the RMS difference is 30 Gt, that is, about 50% larger. For the SE drainage system (see Figures 4 and S2), the best fit of the TUD-SUSTech solutions to the solutions of the analysis centers is obtained for a regularization parameter of 1×10^{-25} (JPL) and 3×10^{-25} (CSR and GSFC), respectively.

In the NE drainage system (see Figures 4 and S2), the dependence of the estimated mass variations on the regularization parameter shows a more complicated behavior. With increasing regularization parameter, the mass loss trend first becomes smaller but increases starting with a regularization parameter of 3×10^{-26}. Minimum RMS differences are attained when choosing regularization parameters of 3×10^{-25} (JPL and CSR) and 1×10^{-24} (GSFC).

In the N drainage system (see Figures 4 and S2), no regularization applied to the TUD-SUSTech solution provides the best fit to the JPL and GSFC solutions, whereas a minor regularization of 3×10^{-26} is necessary to obtain the best possible fit to the CSR solutions.

Overall, the analysis shows that regularization has a significant impact on the estimated mass anomalies. The fit of the TUD-SUSTech solutions to the solutions from CSR, JPL, and GSFC can be optimized by choosing an appropriate regularization parameter when computing the TUD-SUSTech solutions (see Figures 3 and 4). To obtain the smallest RMS difference to the JPL solutions, the least regularization is needed in most cases, whereas a somehow larger amount of regularization is needed to obtain the smallest RMS fit to the CSR and GSFC solutions.

4.2. Numerical Study to Analyze Regularization-Driven Biases in Mascon-Type Estimates

The results of Section 4.1 indicate that the applied regularization is one of the contributors to the observed discrepancies between the CSR, JPL, and GSFC mascon solutions. To further investigate the impact of the regularization, we performed two numerical experiments.

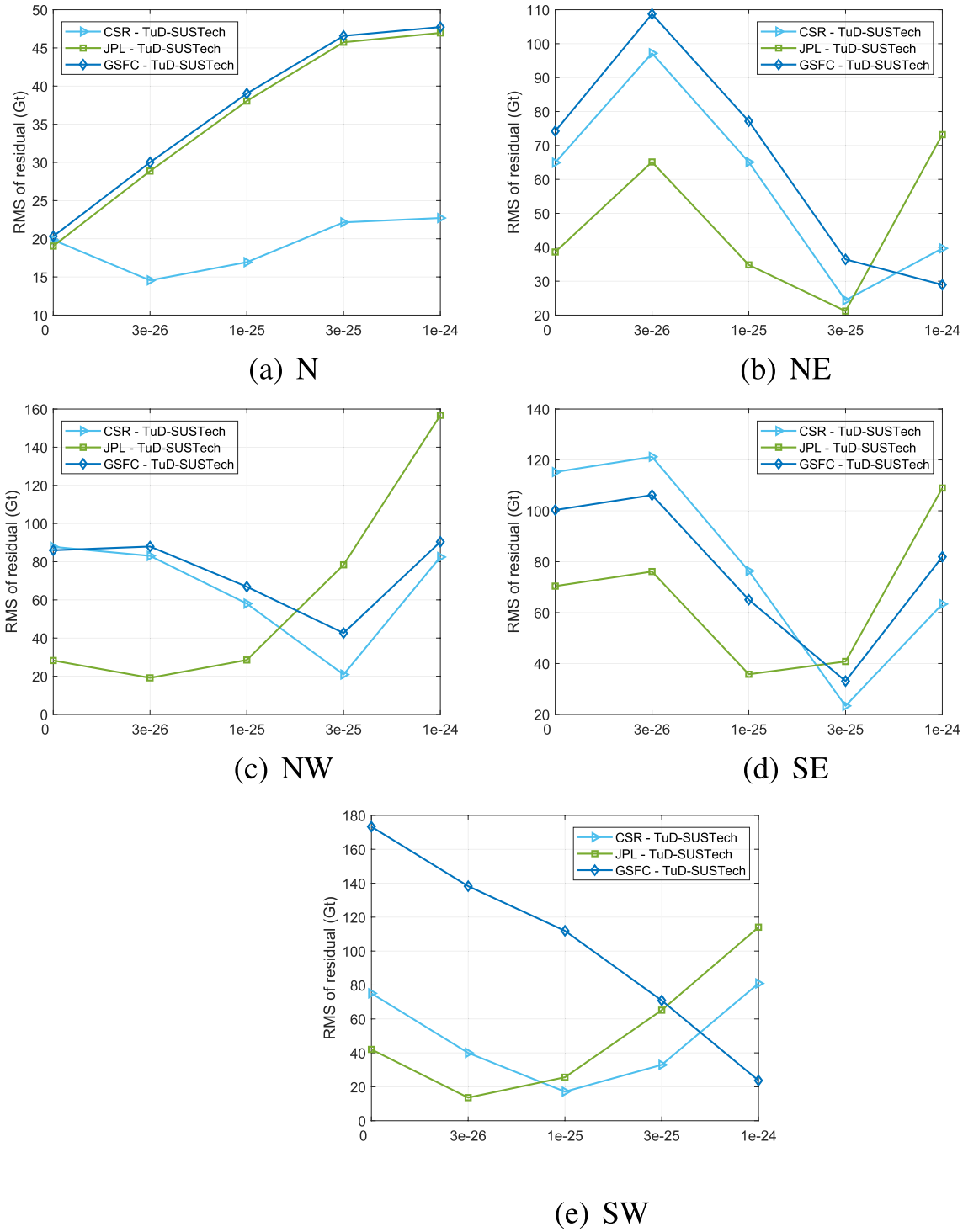

Figure 4. RMS differences between the official (CSR, JPL, and GSFC) monthly solutions and the TUD-SUSTech monthly solutions as functions of the regularization parameter of the TUD-SUSTech solutions.

In the first experiment, mass anomaly time series were computed from a combination of ICESat and RACMO 2.3 data using the approach of Ran, Ditmar, Klees, et al. (2018) and Ran, Ditmar, and Klees (2018). The 20-by-20 km ICESat-based trends were taken from Felikson et al. (2017) and upscaled by a factor of 2.3 to match the trend magnitudes from GRACE data over the period 2004–2014. The 11-by-11 km RACMO 2.3 SMB data, which are available with a temporal resolution of 1 day, were resampled to the 20-by-20 km

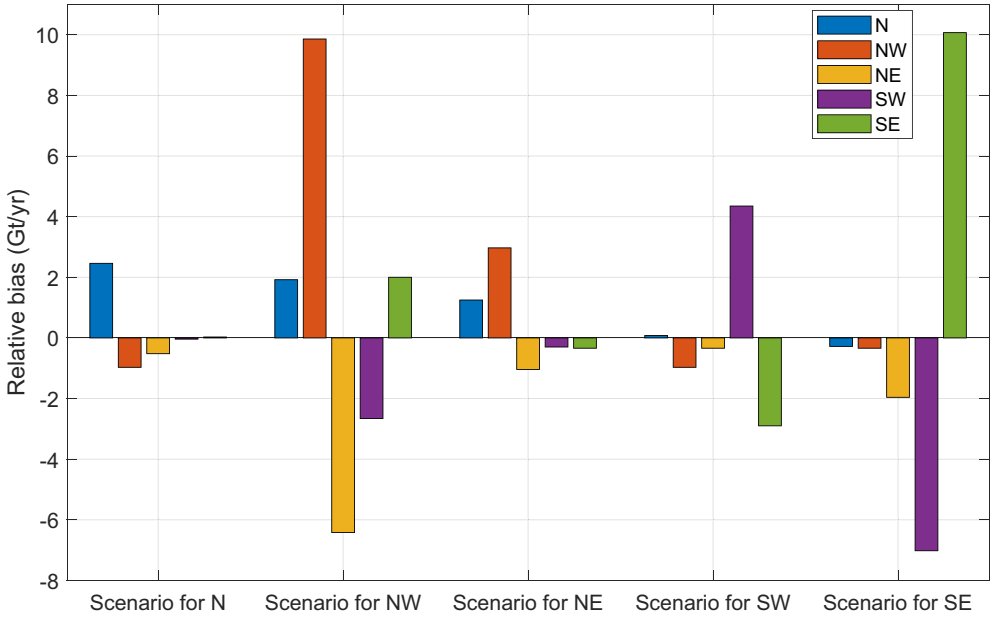

Figure 5. Analysis of relative biases due to signal leakage from one drainage system to the others due to regularization. Note that for every scenario considered, the mass change signal is confined to the drainage system, whereas no mass change is assumed in all other drainage systems. The relative bias is the difference between the solutions computed with regularization parameters of 10^{-25} and 10^{-24}, respectively.

ICESat cells, integrated in time, and time-averaged to provide monthly SMB-related mass anomaly time series. Then, these time series were de-trended, added to the ICESat trends, and spatially integrated to provide monthly mass anomalies per mascon. The mascon definition of JPL was used (cf., Figure 1a). The resulting monthly mass anomaly time series per mascon serves as the true signal. From this signal, pseudo-observations were generated and inverted into monthly mass anomalies using the TUD-SUSTech mascon approach. To investigate the bias caused by regularization, two scenarios were considered, which differ in the choice of the regularization parameter. One scenario uses a regularization parameter of 10^{-25}. This value appeared to be the optimal one according to the L-curve method (Hansen, 1992) when inverting monthly GRACE level-2 data into mass anomalies. The second one was set equal to 10^{-24}; this regularization parameter sometimes appeared to be the one that provided the smallest difference between the TUD-SUSTech solutions and the solutions of the GRACE analysis centers (cf., Section 4.1).

We investigated the bias in trends caused by signal leakage from a particular drainage system into another one. To that end, several runs were completed. In each run, the mass anomalies over all drainage systems except the one under consideration were assumed to be zero. In real data processing, an estimation of the bias triggered by a regularization is problematic. Therefore, to facilitate a comparison with the results of real data processing, we focus below on the differences in bias between the two choices of regularization parameters (referred to as the *relative bias* in this study). The obtained results are shown in Figure 5 and Tables S1–S5.

Table S1 contains the result for the NW drainage system, which has the largest (negative) trend of −148 Gt/yr. It turns out that the bias is negligible (about 1%) for a regularization parameter of 10^{-25}, but increases to about 8% when choosing a regularization parameter of 10^{-24}. Signal from the NW drainage system mostly leaks into the neighboring NE drainage system, whereas leakage to the other drainage systems is a factor of 2–3 smaller. This relative bias is maximum in the NW drainage system itself (−9.9 Gt/yr), followed by the NE drainage system (6.4 Gt/yr). The relative biases in the other drainage systems are much smaller.

The results for the other drainage systems are shown in Figure 5 and Tables S2–S5. To summarize, one could find that signal from the SW drainage system mainly leaks into the SE, whereas there is a negligible leakage to NW, N, and NE. The signal from the SE drainage system mostly leaks into the SW; relative biases in NE and N are small. Signal from NE mostly leaks into NW. Leakage from N is small and mostly goes into

Table 2
The Trend Estimates and Relative Biases Observed in Real Data Processing and in the Numerical Simulations Based on Noise-Free Data

	N	NW	NE	SW	SE
Trend recovered with $\alpha = 10^{-25}$ (real data)	−11.24	−119.99	−3.28	−29.36	−101.99
Trend recovered with $\alpha = 10^{-24}$ (real data)	−10.94	−97.86	−17.49	−40.08	−84.81
Relative bias (real data)	**0.29**	**22.13**	**−14.21**	**−10.72**	**17.18**
Total relative bias (simulations)	**5.43**	**10.55**	**−10.29**	**−5.67**	**8.86**

Note. The units are Gt/yr.

NW. Thus, the signal mostly leaks into the eastern/western neighbor of the current drainage system. This is consistent with the well-known fact that the spatial resolution of GRACE in the east-west direction is poorer than that in the north-south direction.

The relative biases computed in the simulation experiment can be easily compared to the relative biases in real data solutions. To that end, we computed the relative bias per drainage system caused by signal leakage from all other drainage systems. We did so by summing up the relative biases shown in Tables S1–S5 (cf., the fourth row in Table 2). The relative biases obtained in the real data processing are shown in the third row in Table 2. The latter were directly computed as the difference between the solutions with regularization parameters 10^{-25} and 10^{-24}, respectively. We notice a reasonable agreement between the relative biases observed in the simulations and in real data processing. For most drainage systems, the relative bias observed in the simulations can explain 50%–70% of the relative bias in the real data case. Furthermore, the signs of relative biases are consistent for all drainage systems. The remaining discrepancies between the simulations and the real data case are likely caused by the combined effect of noise in real data (which manifests itself as north-south stripes), parameterization (i.e., model) errors, and leakage of signal from outside Greenland.

To support the previous statement, we performed a second numerical experiment, where the pseudo-observations in the ICESat/RACMO simulation were contaminated with realistic errors from various sources: parameterization errors, random noise, errors in the Atmosphere and Ocean De-aliasing model, and leakage of signals from outside Greenland. For details of how to compute these errors, we refer to Ran, Ditmar, Klees, et al. (2018) and Ran, Ditmar, and Klees (2018).

As shown in Table 3, the relative biases in the scenario when noisy data are considered to match the relative biases in the real data case even better than before, except for the N drainage system. In the NW, SW, and SE drainage systems, the relative bias observed in the simulations now explains 60%–80% of the relative bias in the real data case. In the NE, the difference of relative biases between the simulation and real data is just 6%. The large difference in N may be caused by signal leakage from the Canadian Arctic in the simulations.

4.3. Improved Spatial Constraints

4.3.1. Performance Analysis Based on Simulated Data

The analysis of Section 4.2 showed that there is a strong signal leakage between neighboring drainage systems. In reality, there is little correlation between mass variations in different drainage systems. This fact

Table 3
The Trends Estimates and Relative Biases Obtained for Regularization Parameters 10^{-25} and 10^{-24} in the Simulation Where Noisy Data are Considered

	N	NW	NE	SW	SE
Trend recovered with $\alpha = 10^{-25}$ (simulation)	−20.30	−155.20	35.66	−15.76	−118.01
Trend recovered with $\alpha = 10^{-24}$ (simulation)	−11.48	−141.50	20.56	−23.66	−104.50
Relative bias (simulation)	8.83	13.69	−15.09	−7.90	13.52

Note. An ordinary first-order Tikhonov regularization is applied in this study. The units are Gt/yr.

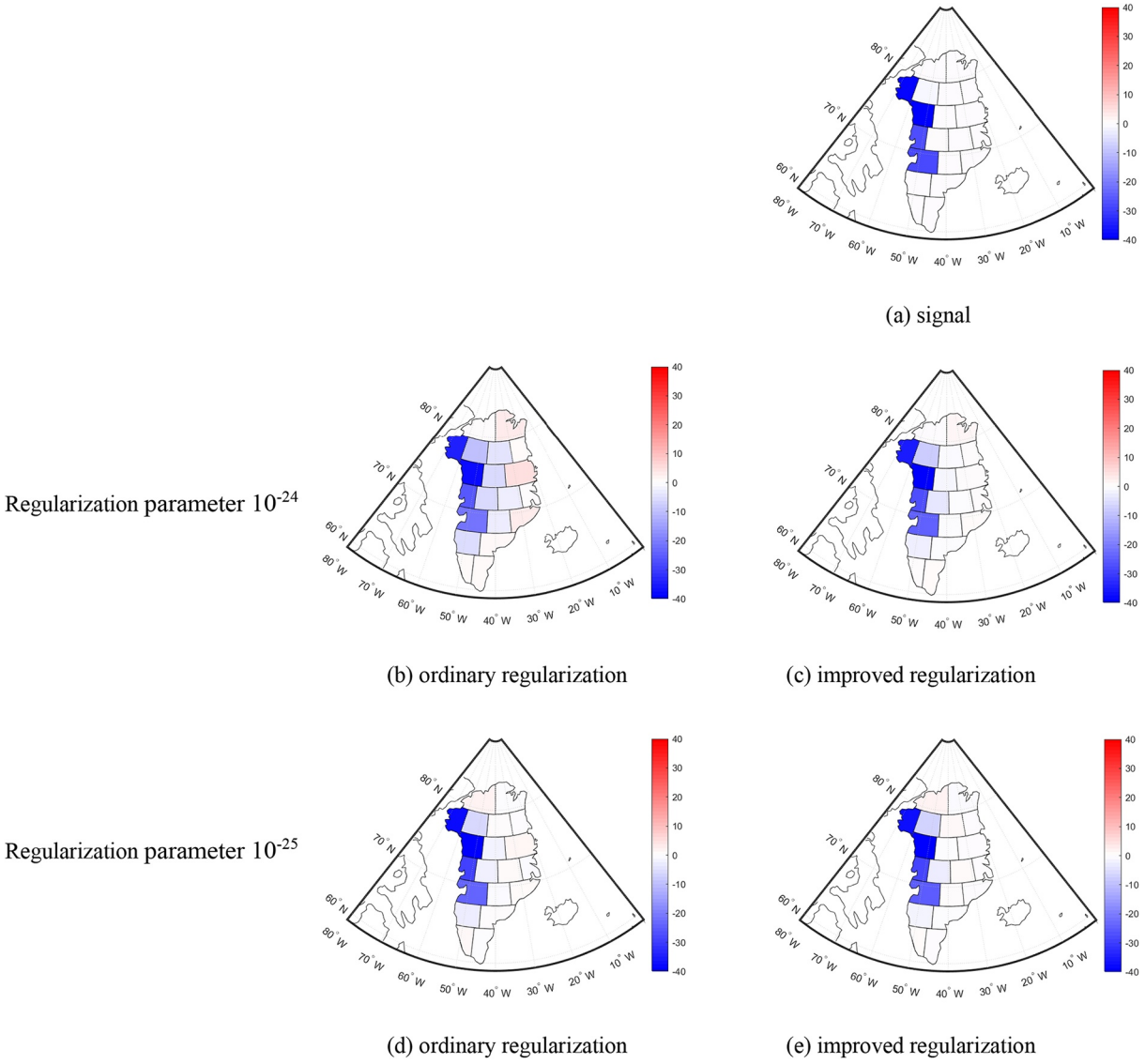

Figure 6. True (panel a) versus estimated trends (panels b–e) for ordinary and improved first-order Tikhonov regularization with two regularization parameters.

was used in the improved first-order Tikhonov regularization approach (cf., Section 2.2). It was expected that it reduces signal leakage between different drainage systems significantly.

To analyze the performance of the data inversion scheme after incorporating the improved first-order Tikhonov regularization, another numerical study is performed. Apart from the improved spatial constraints, the scenarios analyzed correspond to the noise-free synthetic data case of Section 4.2. Our goal is to compare the spatial patterns of the biases caused by the ordinary and improved first-order Tikhonov regularization when the same regularization parameters are used in the two cases. We remind that the term "ordinary" regularization refers to the one that assumes the presence of correlations between neighboring mascons which belong to different drainage system, whereas the term "improved" regularization refers to the case that these correlations are absent.

The "true" trend signal for the NW drainage system is shown in Figure 6a, whereas the estimates obtained with the ordinary and improved spatial constraints and two different regularization parameters (i.e., 10^{-24} and 10^{-25}) are plotted in Figures 6b–6e. In addition, the differences between the estimates and the true trends are shown in Figure 7. We see that the biases when using ordinary spatial constraints are signifi-

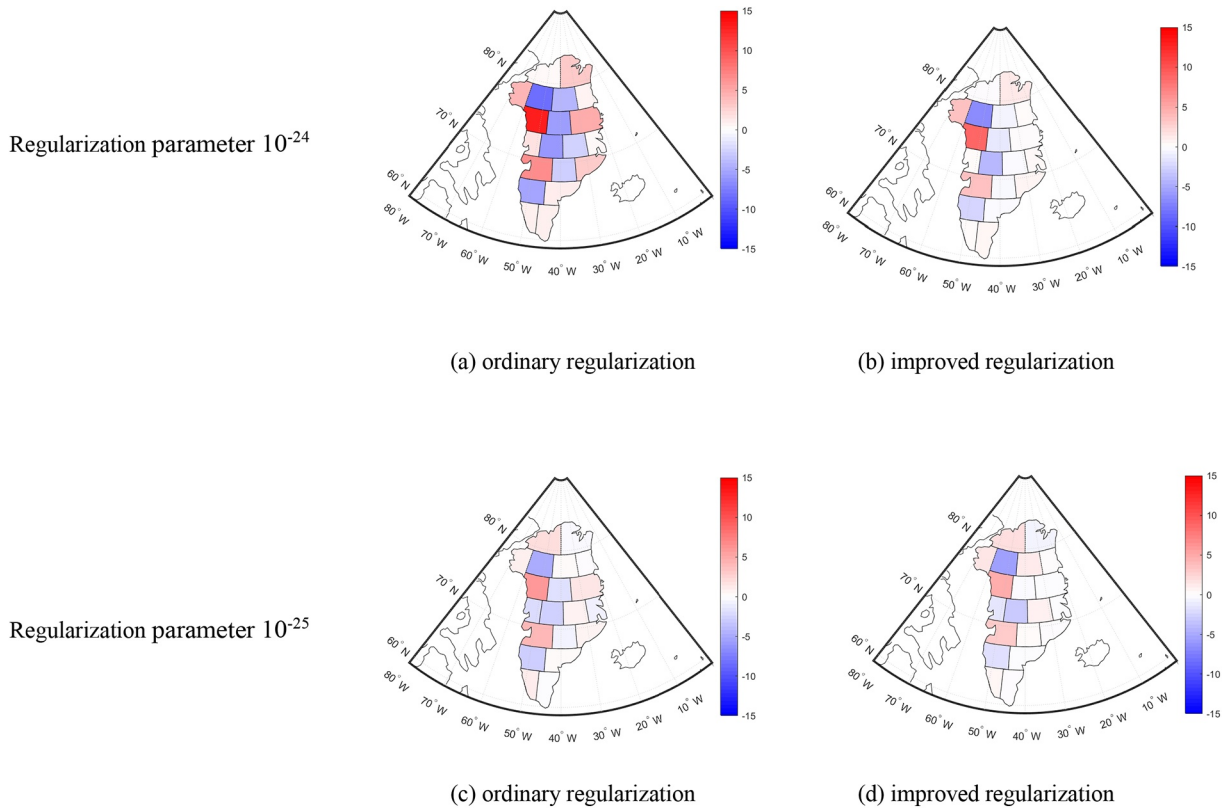

Figure 7. Trend signal of spectral leakage from the NW drainage system for ordinary and first-order Tikhonov regularization with two regularization parameters. The units are Gt/yr.

cantly larger than those when using the improved spatial constraints, especially when the regularization parameter increases from 10^{-25} to 10^{-24}. When the regularization parameter is set equal to 10^{-25}, the RMS of the residuals between the estimated and the true signal per DS decreases by a factor of 15% (namely, from 1.3 to 1.1 Gt/yr) after switching from the ordinary spatial constraints to the improved ones. The reduction becomes even larger when the regularization parameter is increased to 10^{-24} (namely, from 6.4 to 2.8 Gt/yr, i.e., by 56%).

Table 4
RMS Differences Between the Estimated and True Trends-per-Mascon, Reflecting the Biases Caused by the Ordinary and Improved Spatial Regularization

		N	NW	NE	SW	SE
Ordinary	RMS for $\alpha = 10^{-25}$	0.4	1.3	1.9	0.9	2.3
Regularization	RMS for $\alpha = 10^{-24}$	1.5	6.4	3.3	3.1	6.6
Improved	RMS for $\alpha = 10^{-25}$	0.3	1.1	1.7	0.8	2.3
Regularization	RMS for $\alpha = 10^{-24}$	1.2	2.8	4.2	2.4	3.7
Bias	For $\alpha = 10^{-25}$	25%	15%	11%	11%	0%
Reduction	For $\alpha = 10^{-24}$	20%	56%	−27%	23%	44%

Note. The RMS differences are computed per drainage system. In each case, the true signal is limited to only one drainage system, as indicated by the name of the corresponding column. The first and second rows show the RMS biases after the ordinary spatial regularization for the two regularization parameters under consideration. The third and fourth rows present similar information in the case of the improved spatial regularization. The fifth and sixth rows refer to the reduction of these RMS differences when the improved regularization is compared with the ordinary one (a negative number corresponds to an increase in the RMS difference). The unit is Gt/yr.

The results for the other drainage systems are similar (Table 4). In each case, the true signal is limited to only one drainage system, as indicated by the name of the corresponding column. The bias reduction caused by the improved spatial constraints is shown in percentages. The bias reduction stays in most cases at the level of 11%–25%, though may reach 56% when the regularization parameter of 10^{-24} is considered. Note that in the SE, the bias reduction is negligible when the regularization parameter is set to 10^{-25}. This is because the trend estimate obtained with the ordinary regularization (99.03 Gt/yr, see Table 4) is good enough, compared with the true value (99 Gt/yr), and thereby limits the space for further improvements. Besides, the NE shows less accurate trend estimates in the case of the improved spatial constraint under the regularization parameter of 10^{-24}. This is likely caused by an increased mutual compensation of the mass gain signal in the inner NE and the mass loss signal in the coastal NE (see Figure S3). The reason why the other drainage systems do not show such compensation is a homogenous mass loss signal in all the mascons inside those drainage systems.

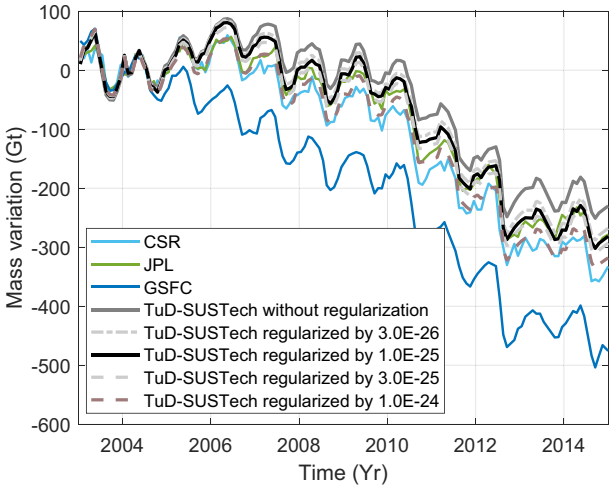

Figure 8. Mass anomaly time series for SW from different mascon solutions. It is similar to Figure 3, but after applying improved first-order Tikhonov regularization, which helps reducing signal leakage from a drainage system to its neighbors.

4.3.2. Performance Analysis Based on Real Data

In this section, the performance of the improved spatial constraints is investigated in the context of the real GRACE data. In Figures 8 and S4, which are similar to Figures 3 and S2 addressed above, the estimates of mass variations per drainage system derived from different mascon products are shown again. This time, the improved Tikhonov regularization was adopted in the TUD-SUSTech mascon solutions. Note that the considered set of regularization parameters is the same as in the analysis based on the ordinary spatial constraints (cf., Figure 3). The optimal regularization parameter found with the L-curve method is 10^{-25} (see Figure S5).

When comparing Figure 8 with Figure 3, we notice that the improved spatial constraints make the estimated mass variations more robust against the choice of the regularization parameter compared to ordinary regularization; that is, the relative biases become much smaller. This is a direct consequence of the reduced signal leakage when using the improved first-order Tikhonov regularization. For instance, in the NW drainage system, the cumulative mass variations from 2003 to 2014 obtained with the smallest (0) and largest (10^{-24}) regularization parameters differ only by about 100 Gt. In contrast, when using the ordinary spatial constraints, the difference was about 230 Gt. Reductions of the relative biases were also found for the other drainage systems.

The trend estimates over 2003–2014 from the CSR, JPL, and GSFC time series, as well as from the TUD-SUSTech time series (computed with both ordinary and improved spatial constraints) are shown in Table 5. The reduced signal leakage of the improved spatial constraints increases the rates of the mass loss in the SE and NW drainage systems with 8 Gt/yr and 4 Gt/yr, respectively, compared with the ordinary spatial constraints. It is also worth noting that the trend estimate for the NE strongly depends on the regularization parameter. In general, the long-term trend estimates for the DSs with the largest mass losses (i.e., NW and SE) are larger in the case of the improved spatial constraints, as compared with those obtained with the ordinary constraints. On the other hand, the former show similar or smaller trend estimates in the other drainage systems, where mass losses are relatively small (i.e., N, SW, and NE). We explain this by the fact that the improved spatial constraints mitigate signal leakage from the drainage systems with the largest mass losses into the drainage systems with small mass losses.

Table 5
Estimated Trends Over 2003–2014 in Gt/yr From Different Mascon Products

				TUD-SUSTech	TUD-SUSTech
	CSR	JPL	GSFC	Improved regularization	Ordinary regularization
N	−19	−23	−23	−17	−16
NW	−102	−114	−103	−120	−116
NE	−15	−10	−16	1	−5
SW	−32	−27	−44	−27	−31
SE	−95	−103	−105	−118	−110
GrIS	−268	−276	−291	−280	−277

Note. TUD-SUSTech solutions are produced with both ordinary and improved spatial constraints under the optimal regularization factor (i.e., 10^{-25}) determined by the L-curve method.

4.3.3. Validation

After the application of the improved spatial constraints to real GRACE data, we validated the obtained estimates with independent data, which is the subject of this section. In general, the absence of knowledge about the true signals makes it difficult to validate GRACE-based monthly estimates. However, it is known that the most reliable way to derive the linear rates of mass variations is to combine many years of GRACE Level 1B data, because this significantly improves the spatial resolution and signal recovery and reduces signal leakage (Loomis, Richey, et al., 2019). Therefore, we use for validating the trend estimates from the GOCO-06S model, which was produced by combining about 15 years (i.e., April 2002 to August 2016) of GRACE data and data from other 19 satellites, including GOCE and SWARM (Kvas et al., 2021). Note that the GOCO-06S trend estimates were determined from GRACE and SLR data only. The other satellite data sets only contributed to the estimation of the static portion of the solution. In addition, the GOCO solution was regularized at high degrees.

Table 6
Comparison of Mass Trend Estimates of the SW Drainage System From Different Mascon Solutions (CSR, JPL, GSFC, and TUD-SUSTech) With Those Based on GOCO-06S Model and the Estimates From Input-Output Method

			TUD-SUSTech		GOCO-06S				IOM
CSR	JPL	GSFC	Improved regularization	Ordinary regularization	60	96	120	200	SMB-ID
−32	−27	−43	−27	−31	−36	−34	−33	−32	−32

Note. The unit is Gt/yr.

In this study, the SW drainage basin is chosen for validation. Among others, this is because there is a rapid mass loss signal in its neighbors, SE and NW. Mass loss estimates in the SW are sensitive to a proper choice of regularization, since they are substantially distorted by signal leakage from its neighbors (see the discussion in Section 4.2). We compute the long-term trend in SW by considering the GOCO-06S SHCs up to different degrees: 60, 96, 120, and 200. A 120-km buffer is introduced to capture the signal leakage into the ocean. The total GOCO-06S based trend in SW decreases from −36 to −32 Gt/yr, when the maximum considered spherical harmonic degree increases from 60 to 200 (see Table 6 and Figure S6). The estimated trend decreases with increasing spatial resolution due to a reduction of signal leakage from the neighboring drainage systems. Note also that the time intervals of GOCO-06S (April 2002 to August 2016) and of the mascon products (January 2003 to July 2016) are slightly different. Therefore, we made an additional test by adjusting the considered time interval of CSR and JPL mascon products to make it exactly the same as the time interval of GOCO-06S. It is found that the inconsistency caused by the differences in time-intervals (January 2003 to July 2016 vs. April 2002 to August 2016) is negligible, that is, at the level of 1 Gt/yr. By comparing different trend estimates, we find that the SW trend from GOCO-06S, CSR, JPL, and TUD-SUSTech are all similar, that is, about −30 Gt/yr, whereas the GSFC trend estimate is much larger: −43 Gt/yr.

The mass balance of the SW drainage system can also be estimated by the Input and Output Method (IOM) as SMB minus Ice Discharge (ID). In SW, the contribution of the latter is relatively small, which implies that errors in ID estimates (e.g., due to unaccounted temporal variations of ice flow velocities) are small as well. This was another reason to select the SW drainage system as the test area. In our study, we combine the SMB trend estimate from the RACMO2.3p2 model, which offers a 1-km spatial resolution at the daily temporal scale (Noël et al., 2021), and the ice discharge estimate from King et al. (2020). The SMB trend in SW over January 2003 to July 2016 is −20 Gt/yr, whereas the ice discharge over the same time interval is 12 Gt/yr. The latter estimate is consistent with that of Mankoff et al. (2020) and Bevis et al. (2019), even though the latter considered a slightly different geometry of SW. Then, based on the IOM, the total mass balance in SW is −32 Gt/yr (see Table 6). This estimate is consistent with those based on CSR, JPL, TuD-SUSTech, and GOCO-06S.

5. Discussion

5.1. Global Mass Conservation

The mascon approach exploited by GSFC, CSR, and JPL, which deals with the GRACE Level-1B data, ensures a global mass conservation during the estimation of a global set of mascons with the relevant constraint equation that the sum of all mascons is equal to zero. The variants of the mascon approach using Level 2 data comply with a global mass conservation implicitly, by assuming that temporal variations of the C_{00} coefficient are equal to 0. As far as the computed mass anomalies are concerned, they are *regional* solutions by definition. A mass conservation in a regional solution is neither ensured nor needed. For instance, a solution ensuring a mass conservation in a region that covers only Greenland and surrounding areas would be totally unphysical. It would be fair to explicitly apply the mass conservation condition only if the mass anomalies were estimated from Level-2 data globally.

5.2. "Improved" Regularization Versus Regularizations Applied to Other Mascon Solutions

The CSR mascon products are estimated by a temporally and spatially variable zero-order Tikhonov regularization. It means that no correlation between mascons is considered in the CSR mascon products. In this

study, we cutoff the correlations for mascons in different drainage systems, but consider the correlations between mascons within the same drainage system. Thereby, our method of regularization is in-between the approach of CSR on the one hand and the approaches of JPL and GSFC on the other hand.

5.3. Added Value of the "Improved" Regularization

Our study shows an added value of the improved Tikhonov regularization, which assumes no signal correlations between pairs of mascons belonging to different drainage basins. Using a set of simulations, we show that the improved regularization mitigates signal leakage between drainage systems by 11%–56%. Then, in the real data analysis, it is also found that for the ordinary Tikhonov regularization, the estimates are quite sensitive to the choice of regularization parameter (see Figure 3), whereas they become more robust if the improved regularization is applied (see Figure 8). For instance, for the improved Tikhonov regularization, the difference between trends over 2003 and 2016 obtained with the smallest regularization factor in Figure 8 (i.e., 3.0E−26) and the largest regularization factor (i.e., 1.0E−24), it is at the level of 7 Gt/yr; for ordinary Tikhonov regularization, the same difference is about 18 Gt/yr.

Our findings somewhat contradict earlier findings in the context of mass anomalies of hydrological origin for small river basins (Croteau et al., 2014). We explain this inconsistency by a relatively high level of random noise in the case of small river basins. Then, a positive effect of a reduced signal leakage is counteracted by an amplification of random noise, which takes place when the available data are insufficiently sensitive to the mass anomalies to be estimated. In other words, when cutting the signal correlations between mascons in different drainage systems, one has to watch a balance between the reduction of signal leakage and an increase in random noise.

6. Conclusions

In this study, the CSR RL06, JPL RL06, and GSFC v2.4 mascon products are investigated in the context of the ice mass balance of individual drainage basins of the GrIS. From the analysis, significant discrepancies between the mass variations accumulated from 2003 to 2014 are found, which reach values of up to 200 Gt depending on the drainage system. To better understand these discrepancies, a set of alternative mascon-type estimates was derived using the mascon approach of Ran, Ditmar, Klees, et al. (2018). These estimates are constrained with a first-order Tikhonov type regularization to suppress noise. It is found that the mass anomalies at the drainage system scale based on CSR RL06, JPL RL06, and GSFC v2.4 mascon products could be well reproduced by the alternative mascon solutions when choosing an appropriate regularization parameter. Thereby, the discrepancies between the CSR RL06, JPL RL06, and GSFC mascon products may the explained by differences in the spatial constraints applied by the analysis centers. The optimal fit to the JPL solutions requires the least amount of regularization.

A numerical study has been performed to investigate the regularization-driven biases (i.e., signal leakage) in trend estimates for GrIS drainage systems. We compare the simulated biases with those observed in our mascon solutions based on real GRACE data. Since the true signal in the context of real data is not known, we propose to evaluate "relative biases," that is, the differences between the estimates obtained with two different regularization parameters. By comparing the relative biases obtained in the simulations and in real data processing, we find that they match each other reasonably well: the former explain in most cases 50%–70% of the latter ones.

To mitigate the bias caused by the regularization, improved spatial constraints have been implemented. The major assumption behind the improved spatial constraints is that there is no correlation between mascons in different drainage systems. Thereby, the mass anomaly estimates obtained with the improved spatial constraints benefit from less signal leakage. Using simulated and real data, we show that the improved spatial constraints mitigate the signal leakage between drainage systems: the reduction is typically at the level of 11%–25%, though may reach 56% when a relatively large regularization parameter is considered.

In addition, trend estimates in the SW drainage system derived from different mascon products are validated using the GOCO-06S model and the IOM (i.e., as SMB-ID). We found (cf., Table 6) that our estimates match well with the values from both alternative data sets.

Remarkably, long-term trend estimates in the DSs with the largest mass losses (i.e., NW and SE) are larger in the case of the improved spatial constraints, as compared with those obtained with the ordinary spatial constraints. On the other hand, the former show smaller trend estimates in the areas of small mass losses (i.e., N, SW, and NE). This is another evidence that the improved spatial constraints mitigate signal leakage from the DSs with large mass losses outwards and thereby reduce distortions of signals in the areas with small mass losses.

It is worth adding that for the latest GSFC RL06 product, temporal constraints are not applied and the regularization matrices are determined from the pre-fit range-acceleration residuals (Loomis, Luthcke, et al., 2019). JPL and CSR processing centers have recently released new variants of the mascon products as well. We will further analyze all these products in a follow-up study.

Data Availability Statement

Data used in this study were requested from the CSR (http://www2.csr.utexas.edu/grace; last accessed: 1 January 2020), NASA JPL (http://grace.jpl.nasa.gov; last accessed: 1 January 2020), and NASA GSFC (https://earth.gsfc.nasa.gov/geo/data/grace-mascons; last accessed: 1 January 2020).

Acknowledgments
The authors appreciate the constructive feedback from the editor, associate editor, and two reviewers. The authors would like to thank the Center for Space Research at the University of Texas at Austin for providing monthly GRACE solutions in terms of spherical harmonic coefficients and mascon products. Jet Propulsion Laboratory (JPL) and Goddard Space Flight Center (GSFC) at the National Aeronautics and Space Administration are acknowledged for their mascon solutions. Noël B. and van den Broeke M. R. are acknowledged for providing the SMB model RACMO 2.3p2. The authors also thank the National Natural Science Foundation of China (41974094, 41874004, and 41774094) for the support.

References

Baur, O., & Sneeuw, N. (2011). Assessing Greenland ice mass loss by means of point-mass modeling: A viable methodology. *Journal of Geodesy*, *85*(9), 607–615. https://doi.org/10.1007/s00190-011-0463-1

Bevis, M., Harig, C., Khan, S. A., Brown, A., Simons, F. J., Willis, M., et al. (2019). Accelerating changes in ice mass within Greenland, and the ice sheet's sensitivity to atmospheric forcing. *Proceedings of the National Academy of Sciences of the United States of America*, *116*(6), 1934–1939.

Bonin, J., & Chambers, D. (2013). Uncertainty estimates of a GRACE inversion modelling technique over Greenland using a simulation. *Geophysical Journal International*, *194*(1), 212–229. https://doi.org/10.1093/gji/ggt091

Chen, J. L., Wilson, C. R., & Tapley, B. D. (2006). Satellite gravity measurements confirm accelerated melting of Greenland ice sheet. *Science*, *313*(5795), 1958–1960. https://doi.org/10.1126/science.1129007

Chen, J. L., Wilson, C. R., Tapley, B. D., & Grand, S. (2007). GRACE detects coseismic and postseismic deformation from the Sumatra-Andaman earthquake, *Geophysical Research Letters*, *34*, L13302. https://doi.org/10.1029/2007GL030356

Croteau, M. J., Loomis, B., Luthcke, S. B., & Nerem, R. S. (2014). Experiments with GRACE global mascon solutions. *AGU Fall Meeting, San Francisco, CA, 17 December 2014*.

Felikson, D., Urban, T. J., Gunter, B. C., Pie, N., Pritchard, H. D., Harpold, R., & Schutz, B. E. (2017). Comparison of elevation change detection methods from ICESat altimetry over the Greenland ice sheet. *IEEE Transactions on Geoscience and Remote Sensing*, *55*(10), 5494–5505.

Forsberg, R., & Reeh, N. (Eds.). (2007). Mass change of the Greenland ice sheet from GRACE. *Gravity field of the Earth – 1st meeting of the International Gravity Field Service* (Vol. 73). Harita Dergisi.

Han, S.-C., Shum, C., Bevis, M., Ji, C., & Kuo, C.-Y. (2006). Crustal dilatation observed by GRACE after the 2004 Sumatra-Andaman earthquake. *Science*, *313*(5787), 658–662. https://doi.org/10.1126/science.1128661

Hansen, P. C. (1992). Analysis of discrete ill-posed problems by means of the l-curve. *SIAM Review*, *34*, 561–580. https://doi.org/10.1137/1034115

Heki, K., & Matsuo, K. (2010). Coseismic gravity changes of the 2010 earthquake in central Chile from satellite gravimetry. *Geophysical Research Letters*, *37*, L24306. https://doi.org/10.1029/2010GL045335

Jacob, T., Wahr, J., Pfeffer, W., & Swenson, S. (2012). Recent contributions of glaciers and ice caps to sea level rise. *Nature*, *482*(7386), 514–518. https://doi.org/10.1038/nature10847

King, M. D., Howat, I. M., Candela, S. G., Noh, M. J., Jeong, S., Noël, B. P. Y., et al. (2020). Dynamic ice loss from the Greenland Ice Sheet driven by sustained glacier retreat. *Communications Earth & Environment*, *1*. https://doi.org/10.1038/s43247-020-0001-2

Kvas, A., Brockmann, J. M., Krauss, S., Schubert, T., Gruber, T., Meyer, U., et al. (2021). GOCO06s – A satellite-only global gravity field model. *Earth System Science Data*, *13*, 99–118. https://doi.org/10.5194/essd-13-99-2021

Landerer, F., & Swenson, S. (2012). Accuracy of scaled GRACE terrestrial water storage estimates. *Water Resources Research*, *48*(4), W04531. https://doi.org/10.1029/2011WR011453

Loomis, B. D., Luthcke, S. B., & Sabaka, T. J. (2019). Regularization and error characterization of GRACE mascons. *Journal of Geodesy*, *93*, 1381–1398. https://doi.org/10.1007/s00190-019-01252-y

Loomis, B. D., Rachlin, K. E., Wiese, D. N., Landerer, F. W., & Luthcke, S. B. (2020). Replacing GRACE/GRACE-FO C30 with satellite laser ranging: Impacts on Antarctic Ice Sheet mass change. *Geophysical Research Letters*, *47*, e2019GL085488. https://doi.org/10.1029/2019GL085488

Loomis, B. D., Richey, A. S., Arendt, A. A., Appana, R., Deweese, Y. J., Forman, B. A., et al. (2019). Water storage trends in high mountain Asia. *Frontiers of Earth Science*, *7*, 235. https://doi.org/10.3389/feart.2019.00235

Luthcke, S. B., Sabaka, T. J., Loomis, B. D., Arendt, A. A., McCarthy, J. J., & Camp, J. (2013). Antarctica, Greenland and Gulf of Alaska land-ice evolution from an iterated GRACE global mascon solution. *Journal of Glaciology*, *59*(216), 613–631. https://doi.org/10.3189/2013JoG12J147

Mankoff, K. D., Solgaard, A., Colgan, W., Ahlstrøm, A. P., Khan, S. A., & Fausto, R. S. (2020). Greenland Ice Sheet solid ice discharge from 1986 through March 2020. *Earth System Science Data*, *12*, 1367–1383. https://doi.org/10.5194/essd-12-1367-2020

Noël, B., van de Berg, W. J., van Meijgaard, E., Kuipers Munneke, P., van de Wal, R. S. W., & van den Broeke, M. R. (2015). Evaluation of the updated regional climate model RACMO2.3: Summer snowfall impact on the Greenland Ice Sheet. *The Cryosphere*, *9*(5), 1831–1844. https://doi.org/10.5194/tc-9-1831-2015

Noël, B., van Kampenhout, L., Lenaerts, J. T. M., van de Berg, W. J., & van den Broeke, M. R. (2021). A 21st century warming threshold for sustained Greenland ice sheet mass loss. *Geophysical Research Letters*, *48*, e2020GL090471. https://doi.org/10.1029/2020GL090471

Panet, I., Mikhailov, V., Diament, M., Pollitz, F., King, G., de Viron, O., et al. (2007). Coseismic and post-seismic signatures of the Sumatra 2004 December and 2005 March earthquakes in GRACE satellite gravity. *Geophysical Journal International*, *171*(1), 177–190. https://doi.org/10.1111/j.1365-246X.2007.03525.x

Peltier, W. R., Argus, D. F., & Drummond, R. (2015). Space geodesy constrains ice age terminal deglaciation: The global ICE-6G_C (VM5a) model. *Journal of Geophysical Research: Solid Earth*, *120*, 450–487. https://doi.org/10.1002/2014JB011176

Ramillien, G., Famiglietti, J., & Wahr, J. (2008). Detection of continental hydrology and glaciology signals from GRACE: A review. *Surveys in Geophysics*, *29*(4–5), 361–374. https://doi.org/10.1007/s10712-008-9048-9

Ran, J. (2017). *Analysis of mass variations in Greenland by a novel variant of the mascon approach* (PhD Thesis). Delft University of Technology.

Ran, J., Ditmar, P., & Klees, R. (2018). Optimal mascon geometry in estimating mass anomalies within Greenland from GRACE. *Geophysical Journal International*, *214*(3), 2133–2150. https://doi.org/10.1093/gji/ggy242

Ran, J., Ditmar, P., Klees, R., & Farahani, H. H. (2018). Statistically optimal estimation of Greenland Ice Sheet mass variations from GRACE monthly solutions using an improved mascon approach. *Journal of Geodesy*, *92*(3), 299–319. https://doi.org/10.1007/s00190-017-1063-5

Ran, J., Vizcaino, M., Ditmar, P., van den Broeke, M. R., Moon, T., Steger, C. R., et al. (2018). Seasonal mass variations show timing and magnitude of meltwater storage in the Greenland Ice Sheet. *The Cryosphere*, *12*(9), 2981–2999. https://doi.org/10.5194/tc-12-2981-2018

Rodell, M., Famiglietti, J., Chen, J., Seneviratne, S., Viterbo, P., Holl, S., & Wilson, C. (2004). Basin scale estimates of evapotranspiration using GRACE and other observations. *Geophysical Research Letters*, *31*, L20504. https://doi.org/10.1029/2004GL020873

Rowlands, D. D., Luthcke, S. B., Klosko, S. M., Lemoine, F. G. R., Chinn, D. S., McCarthy, J. J., et al. (2005). Resolving mass flux at high spatial and temporal resolution using GRACE intersatellite measurements. *Geophysical Research Letters*, *32*, L04310. https://doi.org/10.1029/2004GL021908

Sabaka, T. J., Rowlands, D. D., Luthcke, S. B., & Boy, J. P. (2010). Improving global mass flux solutions from Gravity Recovery and Climate Experiment (GRACE) through forward modeling and continuous time correlation. *Journal of Geophysical Research: Solid Earth*, *115*, B11403. https://doi.org/10.1029/2010JB007533

Sasgen, I., Martinec, Z., & Bamber, J. (2010). Combined GRACE and InSAR estimate of West Antarctic ice mass loss. *Journal of Geophysical Research: Earth Surface*, *115*, F04010. https://doi.org/10.1029/2009JF001525

Save, H., Bettadpur, S., & Tapley, B. D. (2016). High resolution CSR GRACE RL05 mascons. *Journal of Geophysical Research: Solid Earth*, *121*, 7547–7569. https://doi.org/10.1002/2016JB013007

Scanlon, B. R., Zhang, Z., Save, H., Wiese, D. N., Landerer, F. W., Long, D., et al. (2016). Global evaluation of new GRACE mascon products for hydrologic applications. *Water Resources Research*, *52*(12), 9412–9429. https://doi.org/10.1002/2016WR019494

Schmidt, R., Schwintzer, P., Flechtner, F., Reigber, C., Güntner, A., Döll, P., et al. (2006). GRACE observations of changes in continental water storage. *Global and Planetary Change*, *50*(1–2), 112–126. https://doi.org/10.1016/j.gloplacha.2004.11.018

Schrama, E. J. O., & Wouters, B. (2011). Revisiting Greenland Ice Sheet mass loss observed by GRACE. *Journal of Geophysical Research: Solid Earth*, *116*, B02407. https://doi.org/10.1029/2009JB006847

Schrama, E. J. O., Wouters, B., & Rietbroek, R. (2014). A mascon approach to assess ice sheet and glacier mass balances and their uncertainties from GRACE data. *Journal of Geophysical Research: Solid Earth*, *119*, 6048–6066. https://doi.org/10.1002/2013JB010923

Shepherd, A., Ivins, E. R., A, G., Barletta, V. R., Bentley, M. J., Bettadpur, S., et al. (2012). A reconciled estimate of ice-sheet mass balance. *Science*, *338*(6111), 1183–1189. https://doi.org/10.1126/science.1228102

Siemes, C., Ditmar, P., Riva, R. E. M., Slobbe, D. C., Liu, X. L., & Hashemi Farahani, H. (2013). Estimation of mass change trends in the Earth's system on the basis of GRACE satellite data, with application to Greenland. *Journal of Geodesy*, *87*, 69–87. https://doi.org/10.1007/s00190-012-0580-5

Sun, W., Okubo, S., Fu, G., & Araya, A. (2009). General formulations of global co-seismic deformations caused by an arbitrary dislocation in a spherically symmetric earth model-applicable to deformed earth surface and space-fixed point. *Geophysical Journal International*, *177*(3), 817–833. https://doi.org/10.1111/j.1365-246X.2009.04113.x

Sun, Y., Riva, R., & Ditmar, P. (2016). Optimizing estimates of annual variations and trends in geocenter motion and J2 from a combination of GRACE data and geophysical models. *Journal of Geophysical Research: Solid Earth*, *121*, 8352–8370. https://doi.org/10.1002/2016JB013073

Syed, T., Famiglietti, J., Rodell, M., Chen, J., & Wilson, C. (2008). Analysis of terrestrial water storage changes from GRACE and GLDAS. *Water Resources Research*, *44*(2), W02433. https://doi.org/10.1029/2006WR005779

Tapley, B. D., Bettadpur, S., Ries, J. C., Thompson, P. F., & Watkins, M. M. (2004). GRACE measurements of mass variability in the Earth system. *Science*, *305*(5683), 503–505. https://doi.org/10.1126/science.1099192

Tapley, B. D., Watkins, M., Flechtner, F., Reigber, C., Bettadpur, S., Rodell, M., et al. (2019). Contributions of GRACE to understanding climate change. *Nature Climate Change*, *9*(5), 358–369. https://doi.org/10.1038/s41558-019-0456-2

Tikhonov, A. (1963a). On the solution of incorrectly formulated problems and the regularization method. *Soviet mathematics - Doklady*, *4*, 1035–1038.

Tikhonov, A. (1963b). Regularization of incorrectly posed problems. *Soviet Mathematics - Doklady*, *4*, 1624–1627.

van den Broeke, M., Bamber, J., Ettema, J., Rignot, E., Schrama, E., van de Berg, W. J., et al. (2009). Partitioning recent Greenland mass loss. *Science*, *326*(5955), 984–986. https://doi.org/10.1126/science.1178176

Velicogna, I., Mohajerani, Y., A, G., Landerer, F., Mouginot, J., Noel, B., et al. (2020). Continuity of ice sheet mass loss in Greenland and Antarctica from the GRACE and GRACE Follow-On missions. *Geophysical Research Letters*, *47*, e2020GL087291. https://doi.org/10.1029/2020GL087291

Velicogna, I., Sutterley, T. C., & van den Broeke, M. R. (2014). Regional acceleration in ice mass loss from Greenland and Antarctica using GRACE time variable gravity data. *Geophysical Research Letters, Space Physics*, *119*, 8130–8137. https://doi.org/10.1002/2014GL061052

Velicogna, I., & Wahr, J. (2006). Acceleration of Greenland ice mass loss in spring 2004. *Nature*, *443*(7109), 329–331. https://doi.org/10.1038/nature05168

Wahr, J., Molenaar, M., & Bryan, F. (1998). Time variability of the Earth's gravity field: Hydrological and oceanic effects and their possible detection using GRACE. *Journal of Geophysical Research: Solid Earth*, *103*, 30205–30229. https://doi.org/10.1029/98JB02844

Wang, L., Shum, C., Simons, F., Tapley, B., & Dai, C. (2012). Coseismic and postseismic deformation of the 2011 Tohoku-Oki earthquake constrained by GRACE gravimetry. *Geophysical Research Letters*, *39*, L07301. https://doi.org/10.1029/2012GL051104

Watkins, M. M., Wiese, D. N., Yuan, D.-N., Boening, C., & Landerer, F. W. (2015). Improved methods for observing Earth's time variable mass distribution with GRACE using spherical cap mascons. *Journal of Geophysical Research: Solid Earth*, *120*, 2648–2671. https://doi.org/10.1002/2014JB011547

Wouters, B., Chambers, D., & Schrama, E. J. O. (2008). GRACE observes small-scale mass loss in Greenland. *Geophysical Research Letters*, *35*, L20501. https://doi.org/10.1029/2008GL034816